TUDelft

Delft University of Technology

A Spatially Diverse 2TX-3RX Galvanic-Coupled Transdural Telemetry for Tether-Less Distributed Brain-Computer Interfaces

Shi, Chengyao ; He, Yuming; Gourdouparis, Marios; Dolmans, Guido; Liu, Yao-Hong

Important note
To cite this publication, please use the final published version (if applicable).
Please check the document version above.

A Spatially Diverse 2TX-3RX Galvanic-Coupled Transdural Telemetry for Tether-Less Distributed Brain–Computer Interfaces

Chengyao Shi , *Graduate Student Member, IEEE,* Yuming He , *Graduate Student Member, IEEE,*
Marios Gourdouparis , *Graduate Student Member, IEEE,* Guido Dolmans ,
and Yao-Hong Liu , *Senior Member, IEEE*

Abstract—A near-field galvanic coupled transdural telemetry ASICs for intracortical brain-computer interfaces is presented. The proposed design features a two channels transmitter and three channels receiver (2TX-3RX) topology, which introduces spatial diversity to effectively mitigate misalignments (both lateral and rotational) between the brain and the skull and recovers the path loss by 13 dB when the RX is in the worst-case blind spot. This spatial diversity also allows the presented telemetry to support the spatial division multiplexing required for a high-capacity multi-implant distributed network. It achieves a signal-to-interference ratio of 12 dB, even with the adjacent interference node placed only 8 mm away from the desired link. While consuming only 0.33 mW for each channel, the presented RX achieves a wide bandwidth of 360 MHz and a low input referred noise of 13.21 nV/$\sqrt{Hz}$. The presented telemetry achieves a 270 Mbps data rate with a BER $<$ 10^{-6} and an energy efficiency of 3.4 pJ/b and 3.7 pJ/b, respectively. The core footprint of the TX and RX modules is only 100 and 52 mm^2, respectively, minimizing the invasiveness of the surgery. The proposed transdural telemetry system has been characterized ex-vivo with a 7-mm thick porcine tissue.

Index Terms—Body channel communication (BCC), distributed BCIs, galvanic coupling, high speed, intracortical brain-computer interface (iBCI), microelectrode array (MEA), neural interface, spatial diversity, spatial division multiplexing (SDM), transceiver, transdural, wireless telemetry.

Chengyao Shi and Guido Dolmans are with IMEC, 5656 AE Eindhoven, The Netherlands, and also with the Department of Electrical Engineering, Eindhoven University of Technology (TU/e), 5612 AZ Eindhoven, The Netherlands (e-mail: c.shi@tue.nl; g.dolmans@tue.nl).

Yuming He and Marios Gourdouparis are with IMEC, 5656 AE Eindhoven, The Netherlands (e-mail: yuming.he@imec.nl; marios.gourdouparis@imec.nl).

Yao-Hong Liu is with IMEC, 5656 AE Eindhoven, The Netherlands, also with the Department of Electrical Engineering, Eindhoven University of Technology (TU/e), 5612 AZ Eindhoven, The Netherlands, and also with the Department of EEMCS, Delft University of Technology, 2600 AA Delft, The Netherlands (e-mail: yao-hong.liu@imec.nl).

Digital Object Identifier 10.1109/TBCAS.2024.3373172

I. INTRODUCTION

MANY methods exist that allow for the recording of neural signals [1]. Non-invasive methods, such as electroencephalography (EEG) and magnetoencephalography (MEG), enable the recording of neural signals without resorting to surgery. However, these offer limited insight into the brain's neural activity. To offer treatment for neural disorders or to provide a control method for external prosthetics or exoskeletons for patients with paralysis, it is necessary to reach a deeper understanding of the activities that regulate signals in the brain. Invasive recording methods that require implanting recording devices in direct contact with the cerebral cortex, such as electrocorticography (ECoG) or intracortical recording, significantly outperform non-invasive methods in terms of resolution and signal-to-noise (SNR) ratio.

ECoG places electrodes directly on the surface of the cerebral cortex to record electrical activity. A grid of electrodes of a few centimeters in size is implanted under the skull but on top of the cerebral cortex. Intracortical brain-computer interfaces (iBCIs) utilize penetrating neural probes with microelectrode array (MEA) to record extracellular neuronal activities with exceptional spatial and temporal resolutions since an MEA of a few millimeters can have more than 1000's of recording channels.

An alternative to the MEA involves utilizing multiple ultra-low-power micro-implants distributed across a specific brain region [2], [3], [4], [5]. Each implant is equipped with one [2] or a few [3] recording channels, enabling the capture of brain activities over a broader brain area. Despite its broader coverage advantages, this approach also has a few limitations. Due to their extremely constrained volume and energy resources, the maximum number of recording channels that can be supported is also limited. This may not be suitable for many neuroscience or neurotherapeutic applications that require fine spatial resolution in the neural recording. In addition, cortex tissues can easily grow over such micro-implants, thus increasing challenges for certain scenarios where the option of "explantation" is important, i.e., the neurosurgeons should be able to locate and remove these implants when needed.

Novel (e.g., silicon-based [6], [7] or polymer-based [8]) MEAs continuously increase the spatial density and the number of recording channels, producing large amounts of data and
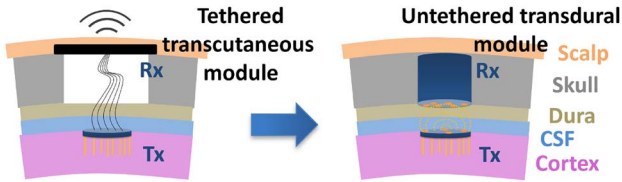
Fig. 1. Proposed untethered transdural BCC telemetry network for intracortical brain-computer interfaces application.

necessitating a wideband in-body telemetry system when fully implanted [9]. Assuming a MEA with a 1000-channel sensing channel, recording at 10-bit resolution and at 25 ksps, the minimum required data rate of the telemetry system reaches 100's of Mbps [6]. While on-chip data compression is investigated, this results in rigid implementations and is unsuitable for complex iBCI research. Furthermore, to enhance patient recovery by minimizing surgical invasiveness, it is important to reduce the footprint of the implant to below ∼10 mm in diameter to accommodate a modern burr-hole craniotomy [10]. Consequently, to mitigate the risk of tissue heating due to a high thermal flux (i.e., power consumption of implant electronics over its area), the power consumption of the telemetry module (typically one of the most power-consuming parts of the implant) should be reduced to a few milliwatts [11].

Existing iBCI systems tether the intracortical MEA on the cortex to the telemetry module in or above the skull [6], [12] (Fig. 1, left). Having wire connections between the telemetry module and the MEA, the latter is bounded in its movements and is not entirely free to follow the brain's motion. Therefore, it will also have relative movements with respect to the brain, causing damage to the surrounding brain tissue. This leads to severe scarring and affects the recording quality and the MEA's longevity [13]. To minimize the glial tissue formation, the MEA on the cortex should be "free-floating [14]." Furthermore, recent "brain-wide" iBCIs [2] distribute multiple MEAs at different brain areas, allowing neuroscientists to map the correlation of neuronal activity across different brain areas.

In this paper, as illustrated in Figs. 1 and 2(a), we aim to design a transdural (between the cortex and the skull, with the channel consisting of cerebrospinal fluid, CSF, and dura with 5-10 mm of total thickness) telemetry network in which each link can tolerate a misalignment up to ±6 mm due to the brain micro-motion [15] and supports network multiplexing for the distributed iBCIs.

An inductive coupled transcranial telemetry network demonstrated in [2] achieves a low power consumption and a small footprint. However, it has a limited data rate due to the narrow resonant bandwidth required for efficient magnetic induction and a limited network capacity due to potential collisions in time-division multiplexed (TDM) random access protocol.

Recent studies on ultra-wideband (UWB) communication [16] demonstrate the great potential of this technology to be employed as a communication system for iBCI due to its ability to achieve high data transfer (1.66 Gbps) with excellent energy efficiency. However, introducing an antenna in the order of 10's of mm² makes it challenging to fit into a communication module
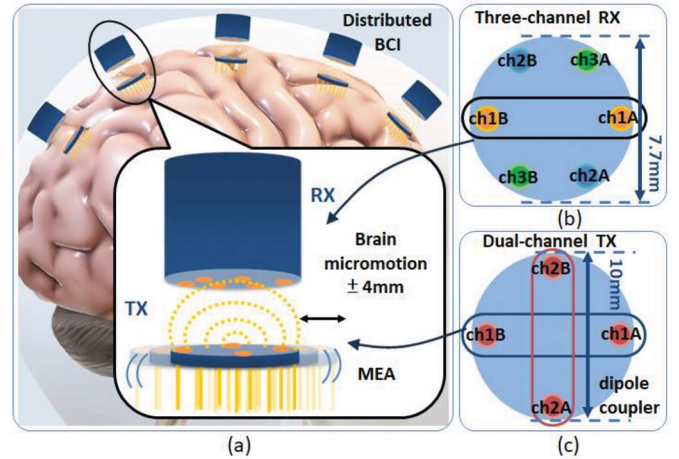
Fig. 2. (a) The concept illustration of the distributed galvanic coupled telemetry network with 2TX-3RX architecture for distributed intracortical brain-computer interface applications. (b) Dipole couplers arrangement for three-channel RX, (c) dipole couplers arrangement of two-channel TX.

within the targeted skull-hole dimensions (<10 mm diameter). In addition, using UWB as the wireless communication for distributed implants requires dividing the frequency band into multiple narrower channels for frequency-division multiplexing (FDM). The transmission bandwidth of each implant is consequently reduced, and the power consumption is significantly increased (∼10 mW in [16]) associated with a more precise carrier frequency generation required for FDM.

It has been demonstrated in [14] that the galvanic-coupled body channel communication (BCC) TX can overcome this challenging trade-off between power, size, and bandwidth. However, the telemetry system in [14] only focused on the TX module, while the full wireless link with a miniature and energy-efficient RX module was not demonstrated. In addition, there is no investigation or mitigation of potential blind spots (detailed in Section II) in [14], where the received signal undergoes severe attenuation.

In this work, we aim to investigate the misalignment and blind spot challenges in transdural BCC and introduce a solution. Furthermore, a novel method for a multi-node brain-wide-distributed network is proposed. A transdural communication link that utilizes the BCC with a proposed topology of a two-channel transmitter and a three-channel receiver (2TX-3RX) provides "spatial diversity", which can mitigate the blind spots and support spatial division multiplexing (SDM). As shown in Fig. 2(b), the two dipole couplers in the TX unit are arranged orthogonally from each other, while the three dipole couplers in the RX are arranged 60 degrees apart. The concept of the proposed architecture is illustrated in Fig. 2, where the TX and the RX are shown with their corresponding dipole couplers. The specific 2TX-3RX configuration was chosen over other alternatives, e.g., 3TX-4RX, because of the optimum trade-off between the minimum required number of channels (thus power consumption) and the required spatial diversity (thus the effectiveness of SDM and misalignment mitigation).

The paper is organized as follows: Section II describes the multi-node distributed telemetry based on SDM. The blind spot
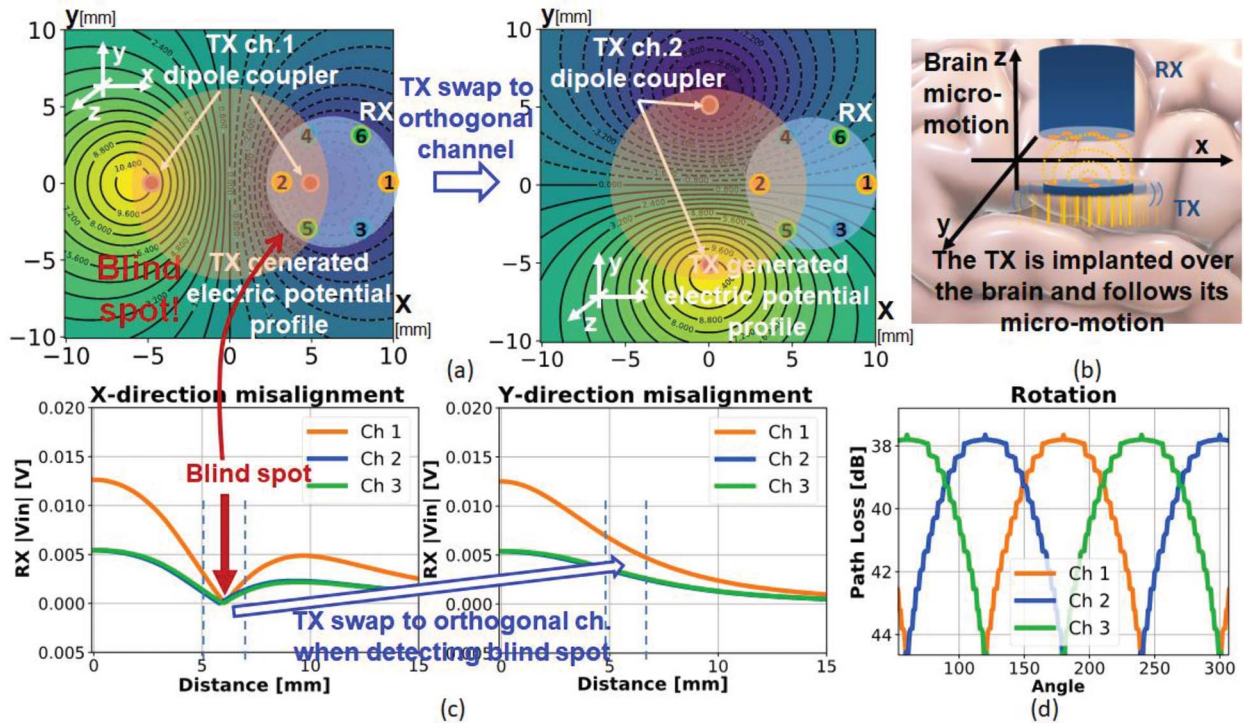
Fig. 3.   The influence of lateral and rotational misalignment on path loss. (a) The electric potential at the receiver's plane is generated by the transmitter's dipole coupler at a 7 mm distance (in the z-axis). (b) Illustration of the brain micromotion. (c) Simulation result for lateral misalignment. (d) Simulation result for rotational misalignment.

issue and multi-node transmission are studied, and an approach is presented. Section III describes the circuit implementation of the 2TX-3RX transceiver topology. Section IV describes the measurement setup, and Section V discusses the measurement results. Finally, in Section VI, we provide the conclusion.

II. THE PROPOSED DISTRIBUTED TRANSDURAL TELEMETRY

The 2TX-3RX transdural BCC telemetry proposed in this work mitigates both the rotational misalignment and solves the blind spot issue, as illustrated in Fig. 2. The subdural implant, consisting of a neural probe and a two-channel BCC TX, is placed on the surface of the cortex, and a three-channel RX placed in the skull cavity. The channel between the two implants consists of a layer of cerebrospinal fluid (CSF) and a layer of dura, for which the frequency response has been extensively studied [14], [17], [18], [19]. The recorded intracortical neural activity from the MEA is amplified and digitized on the subdural implant by the analog front end (AFE) and the ADC. The BCC power amplifier (PA) modulates the data with biphasic pulse modulation and transmits it differentially.

A. Data-Assisted Misalignment Mitigation

Fig. 3 illustrates the operation principle of the proposed data-assisted misalignment mitigation. Misalignments between the TX and RX are unavoidable due to the brain micromotion with respect to the skull (± 4 mm) [15]. On top of that, misalignment introduced from surgical implantation and the potential changes

in brain shape due to aging can lead to even more significant misalignments (up to ± 7 mm). This leads to a severe degradation in the link quality due to a specific electric potential profile of the near-field galvanic coupling, and in the worst case, could even require another surgery to re-establish the lost connection. Consequently, the BCC telemetry must be able to adjust to the misaligned channel characteristics.

A finite element model of the human head is developed in COMSOL^{TM} Multiphysics software using the AC/DC electric current module. The quasi-static approximation is used to compute Maxwell's equations. In the examined telemetry system, the coupling distance, i.e., the distance between the TX and the RX, is approximately 10 mm. At a frequency of 270 MHz, the signal wavelength is 100-140 mm for CSF and dura tissue. Consequently, the conditions necessary for applying the quasi-static approximation are satisfied. The simulated electric potential profile generated by the TX dipolar coupler, as viewed from the RX x-y plane (with z representing the coupling distance), and the relative RX position are shown in Fig. 3. The simulation result of the received signal degradation for lateral (both x and y direction) and rotational misalignments between the TX and RX are shown in Fig. 3(c) and 3(d) respectively. When the lateral misalignment along the x-axis direction falls between the range of 5-7 mm (in parallel to the dipole coupler), a "blind spot" occurs where the dipole coupler closely aligns with one of the equipotential lines, resulting in a significant degradation of the differential received signal amplitude. A mitigation method is proposed, which utilizes the orthogonal channel of the transmitter (TX) when all three receiver channels simultaneously detect
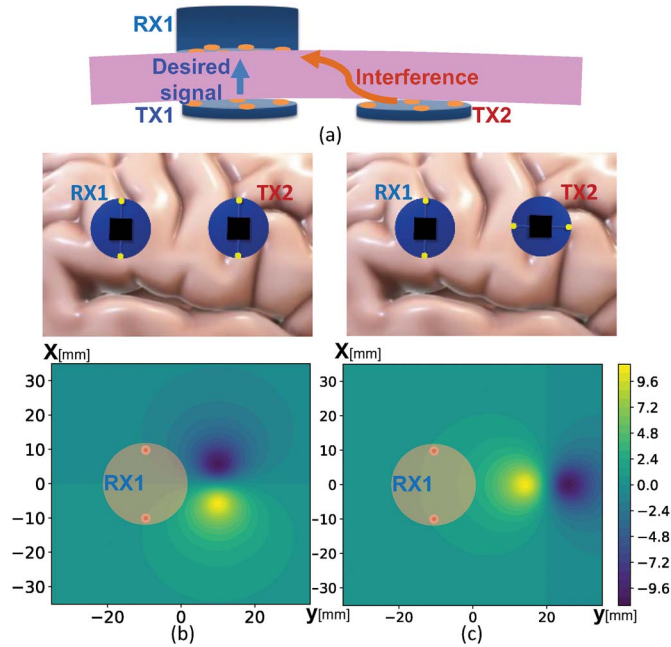
Fig. 4. (a) The illustration of two adjacent telemetry link, one as desired and another one as interference. (b) Electrical potential plot with a parallel configuration of dipole couplers for TX2 and RX1. (c) Electrical potential plot with an orthogonal configuration of dipole couplers for TX2 and RX1.

a low signal strength. This strategy can recover the received signal, as shown in Fig. 3(c).

Similarly, rotational misalignment can also introduce severe path loss. The 3-channel RX with the dipole coupler 60 degrees apart from each coupler is proposed to mitigate the rotational misalignment. At least one TX/RX pair will have less than 30-degree angle misalignment, and the overall loss due to rotation misalignment can be reduced to <2 dB.

Note that the RX is designed to have a sufficient gain range (~30 dB in this work), ensuring the signal amplitude information can be preserved for blind spot and misalignment detections. The RX gain in three channels is tuned simultaneously to avoid saturation.

B. Distributed Telemetry With Spatial Division Multiplexing (SDM)

In conventional EM-based communication (e.g., [16]), the proximity of nodes can introduce interference. Frequency or time division multiplexing (FDM or TDM) are typically employed because of their low complexity, but resulting in significantly reduced telemetry bandwidth for each node when the number of nodes increases [2]. Thanks to the characteristic of near-field galvanic coupling that the electric field signal strength diminishes cubically over distance [20], spatial division multiplexing (SDM) can be employed in the telemetry network by leveraging such a confined electric potential profile. However, when two nodes are very close, e.g., <10 mm, the transmission signal from the adjacent node can still interfere with the desired link, degrading the signal-to-interference ratio (SIR). Fig. 4(a) shows two separate BCC links, the desired link (TX1 to RX1) and the adjacent link (TX2 to RX2), where TX2 becomes the
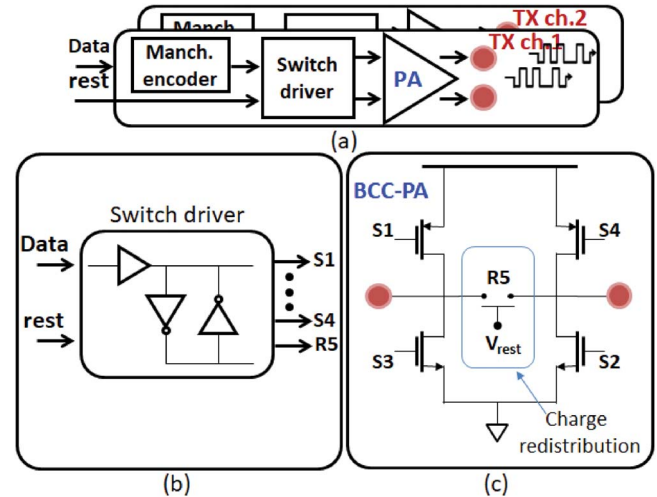
Fig. 5. (a) Block diagram of the two-channel BCC transmitter. (b) Block diagram of the switch driver. (c) The circuit of the BCC-PA contains the H-bridge and the charge redistribution circuit.

interference of the desired link. This work further leverages the propagation property of the orthogonality between two adjacent TXs with different dipole coupler directions to suppress the level of interference from adjacent nodes. By arranging the dipole coupler channel of the TX1 to be orthogonal to that of the TX2 and RX2, assuming TX1's and RX1's dipole coupler direction is already aligned, the interference signal from TX2 received by the RX1 dipole coupler has the same polarity. Given the differential nature of the BCC RX, the signal from TX2 becomes a common mode interference and can be consequently rejected. Note that the RX should be designed to have a > 10 dB Common-Mode Rejection Ratio (CMRR) such that it can drastically reduce the cross-coupling between adjacent nodes. This allows the distance between nodes to be even shorter than 10 mm, enabling a brain-wide implant network with higher spatial density.

III. CIRCUIT IMPLEMENTATION

This section presents the circuit implementation of the two-channel TX and three-channel RX.

A. TX Circuit

The proposed BCC transmitter circuit is shown in Fig. 5. The two channels are identical, and the data is routed based on the active channel. The TX employs an H-bridge topology with an active charge redistribution circuit, and only one of the two TX channels will transmit at a specific time.

The Manchester encoder processes incoming data before passing it to the switch driver. In the presence of incoming data, the switch driver modulates the data using biphasic pulse modulation and sends the control signal to the H-bridge for transmission. In the absence of input data, the switch driver activates the charge redistribution circuit to redistribute any accumulated charge. The switch driver is designed to prevent undefined states (S1 and S3 are on simultaneously, or S2 and S4). Such

undefined states can create a low-resistance path that might introduce a high transient current.

Compared to the author's prior work [14], the current transmitter incorporates a Manchester encoder, along with biphasic modulation implemented by the switch driver, while the BCC-PA is maintained with the same topology.

Safety requirements are crucial for implantable devices. Body channel communication involves transmitting information using electrical currents across tissue layers of dura and CSF. In the design of the H-bridge power amplifier, the primary requirement is to achieve the highest transmission bandwidth and efficiency. Hence, circuit topologies that could maintain a better charge balance, such as the circuit topology with a common current bias, are not adopted [21]. Although the symmetry between NMOS and PMOS in the design has been considered, process and supply variations can still lead to an imbalance in charge between the positive and negative phases during the biphasic pulse transmission, resulting in charge accumulation in the tissue. Since the pulse period for this BCC communication is much shorter than a typical electrical neural stimulator (few nanoseconds vs 100's of microseconds), the charge accumulation is less prominent. In order to ensure absolute safety, two methods are further adopted to prevent charge accumulation on the tissue during transmission [22], [23]. First, a Manchester encoder ensures that the transmitted data remains DC-balanced. Second, an active charge redistribution circuit (Fig. 5(c)) is implemented, which activates at the end of communication to redistribute any accumulated charge.

[24] suggests Eq. (1) to correlate the injected charge with the charge density per surface, aiming to calculate a parameter (k) to determine whether the electrical stimulus can cause damage to the tissues. According to equation (1), the safe range for electric charge flow within the tissue is when the k value remains below $k = 1.85$.

$$\log\left(\frac{Q}{A}\right) = k - \log(Q) \qquad (1)$$

This calculation considers factors such as dipole area (A), the current ($Q = I \times t$), and pulse width (t). The calculated $\grave{k}$ value based on this work has a safety margin of $\Delta k = k - \grave{k} = 10$ from the established safety value, suggesting the charge flow remains well below the safety threshold.

B. RX Circuit

Fig. 6 shows the proposed BCC RX circuit. To maximize RX bandwidth up to 100's of MHz while keeping low power consumption, multiple amplifier stages are designed with resistive loads and cascode transistor topology. The first stage is a low-noise amplifier (LNA), followed by two programmable gain amplifier (PGA) stages using the source degeneration topology to maximize the linear range.

Each stage is AC-coupled to the next stage for rejecting low-frequency common-mode noise, e.g., due to charge accumulation or body noise. It is important to note that BCC has been demonstrated in the literature to be sensitive to FM interference [25], [26], [27], [28], [29]. A narrow-band BCC RX in [30]
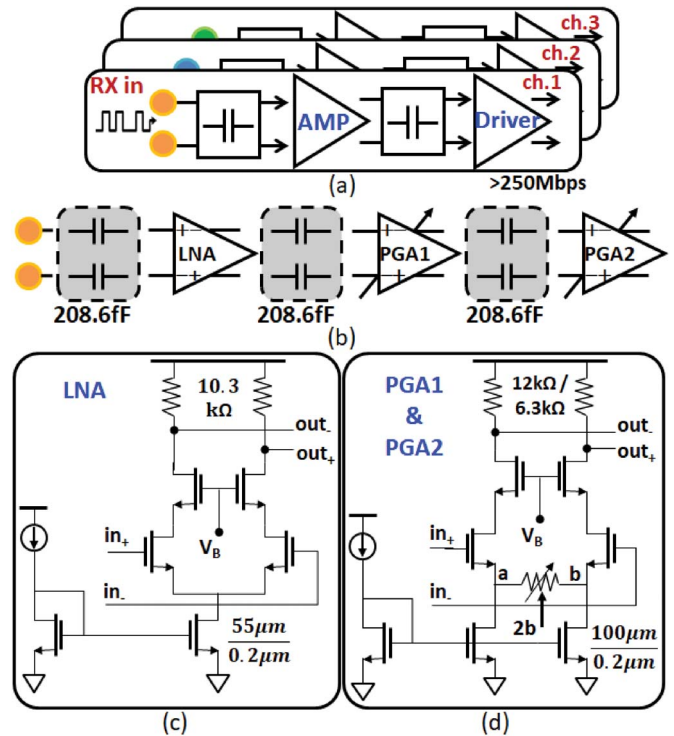
Fig. 6. (a) Block diagram of the three-channel BCC receiver. (b) Block diagram of one receiver's channel. (c) Circuit of the LNA. (d) Circuit of the PGA1 and PGA2.
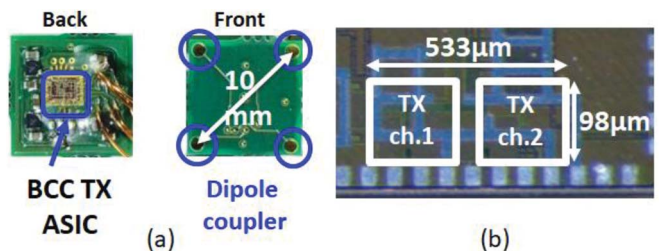
Fig. 7. (a) A picture of the TX PCB with the two pairs of dipole coupler. (b) The micrograph of the two-channel TX ASIC.

mitigates FM interference by avoiding FM bands (88-108 MHz), but this is not feasible for our proposed wideband BCC RX. To ensure the proposed RX has sufficient FM rejection, the biasing tail of each amplifier stage is sized to offer good common-mode rejection up to 110 MHz.

IV. MEASUREMENT RESULTS

This section presents the characterization setup and results of the transceiver ASICs, including the ex-vivo validation with porcine tissue. Additionally, the measurements of misalignment and spatial isolation are performed and described in this section.

A. ASIC Characterization

Both TX and RX ASICs are fabricated with 65 nm CMOS technology. The chip micrograph and the PCB module for the TX and RX are shown in Fig. 7 and Fig. 8, respectively. The TX
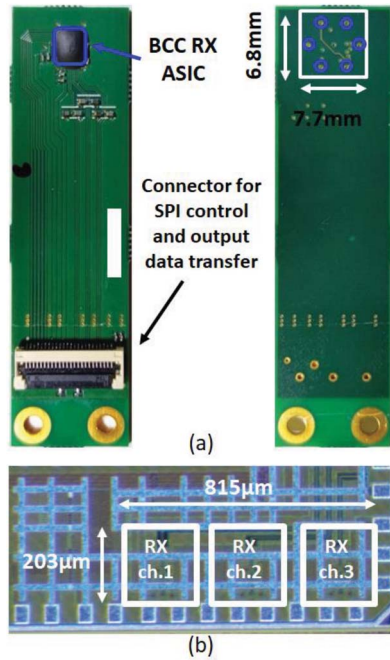
Fig. 8. (a) A picture of the RX PCB with three pairs of dipole coupler. The connector is for SPI control and output data transfer. (b) The chip micrograph of the three-channel RX ASIC.

PCB includes the TX ASIC on the top layer and two pairs of printed dipole couplers on the bottom layer. The RX circuit board includes the RX ASIC on the top layer and three pairs of printed dipole couplers on the bottom layer. The TX and the RX PCBs have a core footprint of 10 mm × 10 mm and 7.7 mm × 6.8 mm, respectively.

The measured RX electrical properties are shown in Fig. 9. The RX covers a wide frequency range from 8 MHz to 370 MHz, with a maximum gain of 21.6 dB. The RX has 49 dB measured CMRR up to the frequency range of the FM band and $\sim$40 dB at 300 MHz. While consuming only 0.33 mW for each channel, the RX achieves a low input referred noise of 13.21 nV/$\sqrt{Hz}$. The TX consumes 0.92 mW. With a maximum bit rate of 270 Mbps, which is primarily limited by the RX bandwidth, the energy efficiency is 3.4 pJ/bit and 3.7 pJ/bit, respectively, for the TX and RX. The power consumption breakdown of the RX is shown in Fig. 10. The main contributor to the RX power consumption is the PGA2 (44%) because of the challenging balance between the bandwidth and the output linearity. The RX output linearity is important in the proposed misalignment mitigation method, which requires preserving amplitude information.

Fig. 11(a) shows an ex-vivo communication link measurement using a porcine tissue with approximately 7 mm thickness. The TX and RX PCBs are coated with non-conductive epoxy during the ex-vivo test. To ensure the accuracy and reliability of BCC propagation property, the ground loop between TX and RX must be avoided. Galvanic isolation between the TX and RX is considered [31], [32] by powering the TX from a laptop with its battery instead of an AC mains supply.

Fig. 11(b) shows the measured eye diagram at the maximum bit rate of 270 Mbps. The measured Bit Error Rate (BER) is less than 10^{-6}. For binary modulation, a BER of 10^{-6} requires an
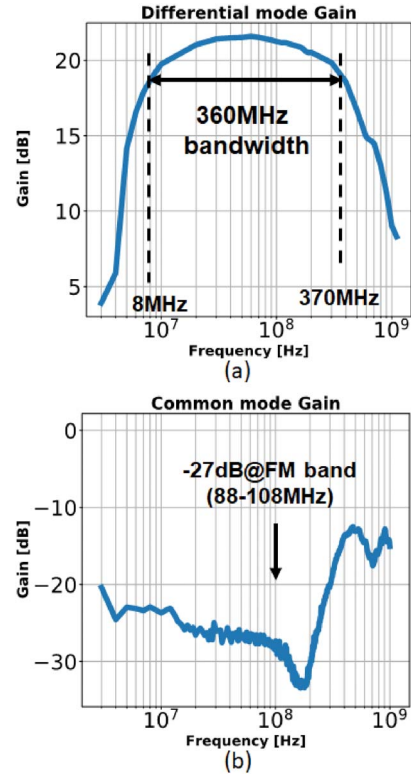
Fig. 9. Characterization of the RX ASIC. (a) The differential mode gain and (b) the common mode gain of the RX ASIC.
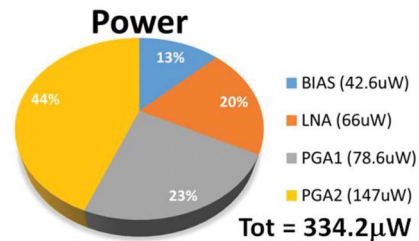
Fig. 10. The power breakdown chart of the RX ASIC.

Eb/No of $\sim$10.6 dB. Considering the use of Manchester coding, the SNR requirement at the RX output is, therefore, 7.6 dB. With the measured receiver's input-referred noise of 13.21 nV/$\sqrt{Hz}$ and the bandwidth of $\sim$360 MHz, the minimum amplitude of the received signal (Vrx$_{RMS}$) satisfying this SNR is 0.6 mV$_{RMS}$. With a transmitting signal amplitude of 0.7 V$_{RMS}$ in this work, and a path loss of $\sim$45 dB measured under the perfect alignment condition, the received signal strength is estimated to be $\sim$4 mV$_{RMS}$. This allows the presented transdural wireless link to meet the target BER requirement of 10^{-6} with abundant margin ($\sim$16 dB), which is important to accommodate various misalignment scenarios (to be detailed in Section IV-B) and coupling distance.

B. Misalignment and Blind Spot Measurements

The measurement setup for misalignment characterization is shown in Fig. 12. A 3D-printed structure and a moving stage with a resolution of 0.1 mm are used to verify and characterize
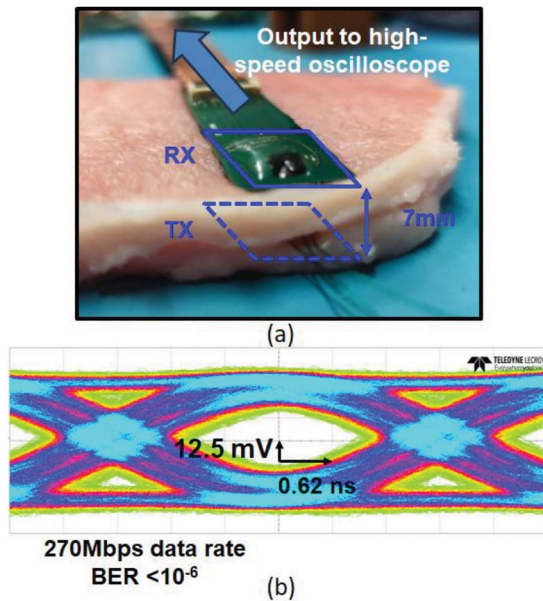
Fig. 11. (a) Picture of the ex-vivo measurement setup. The thickness of porcine tissue is about 7mm. Two separate battery-powered notebooks supply the TX and the RX to ensure galvanic isolation. (b) The measured eye diagram at 270Mbps with porcine tissue. The measured BER is $<10^{-6}$.
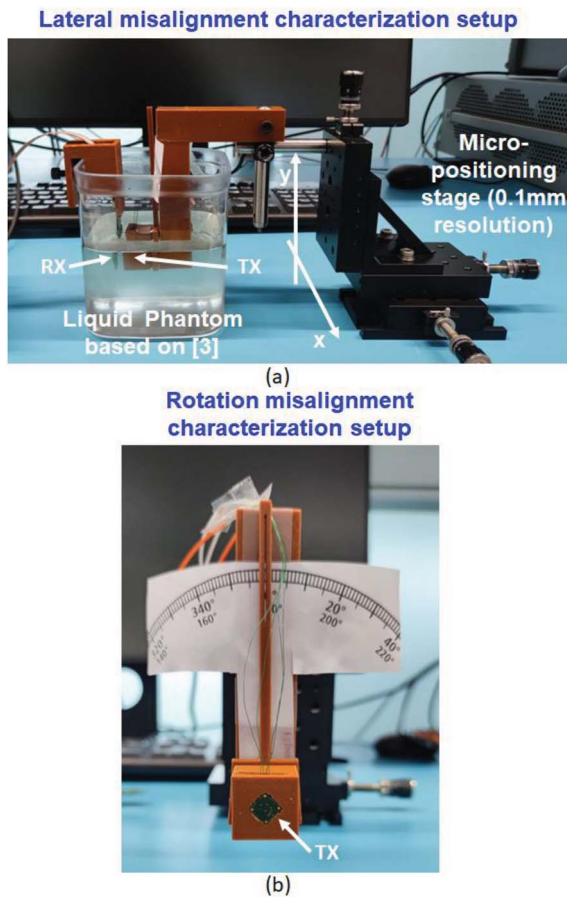
Fig. 12. (a) Picture of the measurement setup for lateral and rotation misalignment. The RX is fixed on the left side of the box, while the TX is connected to the micro-positioning stage on the right. The lateral misalignment characterization is conducted with a 1 mm step, while (b) the rotational misalignment is conducted with a 10-degree step.
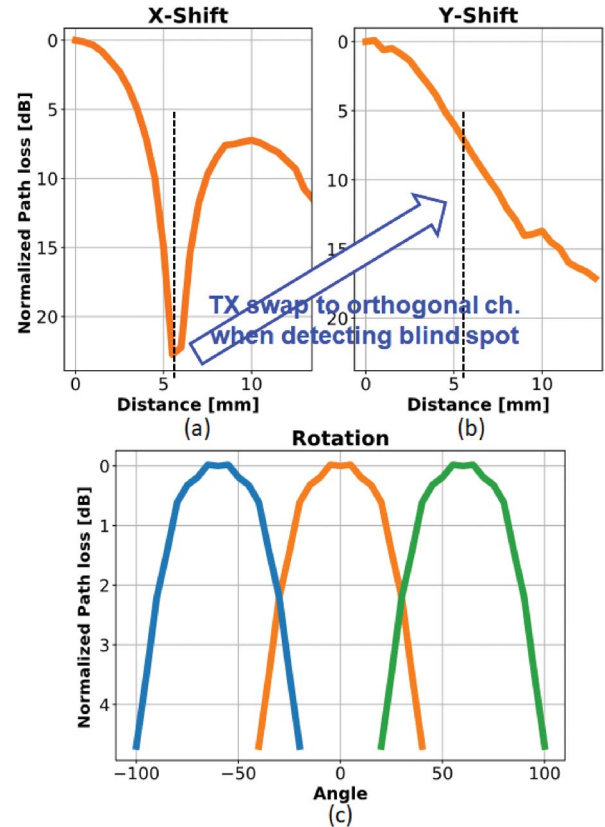
Fig. 13. Ex-vivo measurement result for horizontal misalignment in (a) x-axis direction and in (b) y-axis direction. The blind spot region causes more than 20 dB signal degradation. (c) Measurement result for rotational misalignment.

the path loss under various misalignment conditions. The TX and RX modules with adjustable position and rotation are placed in a liquid phantom, similar to the setup in [14]. The misalignment characterization is conducted by moving the position of the TX each time with a 0.1-mm step for lateral misalignment in both x and y directions and a 10-degree step for rotational misalignment.

The measured path loss for lateral misalignment is shown in Fig. 13(a) and 13(b) for the x and y direction, respectively. The results are normalized with respect to the perfect alignment condition, which has a measured path loss of ~45 dB with a coupling distance of 7 mm. The measurements were carried out independently using a single TX. There is no misalignment in the y-axis while evaluating the displacement along the x-axis, and vice versa. The results reveal that the blind spot is located at ~6 mm lateral misalignment in the x direction, having a > 20 dB higher path loss (Fig. 13(a)). The proposed mitigation method, by swapping it to the orthogonal TX dipole coupler, can recover the path loss by ~13 dB, as shown in the measurement result in Fig. 13(b).

The measurement presented in Fig. 13(c) demonstrates that the proposed 3-channel RX can reduce the path loss due to rotational misalignment to a maximum degradation of only 2 dB. The measured results of both lateral and rotational misalignment match well with the simulation result shown in Fig. 3.

TABLE I
BENCHMARK WITH THE STATE-OF-THE-ART TRANSDURAL OR TRANSCRANIAL TELEMETRY TRANSCEIVER FOR BCI APPLICATIONS

	This Work		Nature ele.'21 Lee [2]	TMTT'22 Shi [14]	JSSC'20 Jang [30]		JSSC'22 Lee [33]		ISSCC'22 Song [16]
Type	**Implant ⟷ implant**		Implant ⟷ wearable	Implant ⟷ implant	Implant ⟷ wearable		Implant ⟷ wearable		Implant ⟷ wearable
Technology	65 nm		65 nm	28 nm	180 nm		180 nm		28 nm
Propagation modality	Near-field galvanic BCC		Inductive coupling	Near-field galvanic coupling	Capacitive BCC		Capacitive BCC		IR-UWB
Modulation	Biphasic pulse		BPSK	Tri-level RZ	FSDT/QPSK		Tri-level RZ		4PPM + 8PSK+ 4PAM impulse
Max. bandwidth	**360 MHz**		NA	250 MHz	42 MHz		NA		NA
Carrier freq.	Baseband		1 GHz	Baseband	168 MHz		40.96 MHz		6–9 GHz
Data rate	**270 Mbps**		10 Mbps	250 Mbps	105 Mbps		20.48 Mbps		1.66 Gbps
RX input ref. noise	13.21 nV/$\sqrt{Hz}$		98.39 nV/$\sqrt{Hz}$	NA	NA		13 nV/$\sqrt{Hz}$		–
Spatial isolation for SDM	**Yes**		No	NA	No		No		No
Misalignment & blind-spot mitigation	**Yes—2TX3RX**		No	No	–		–		–
FM rejection	**Yes (49 dB rejection)**		No	No	Yes		No		–
Tissue thickness	7 mm		8 mm	10 mm	NA		10 cm		15 mm
BER	<1E-6		1E-3[A]	1E-6	–		–		<1E-4
TX/RX ASIC	TX	**RX**	TX	TX	TX	RX	TX	RX	TX
Module area	$10 \times 10 mm^2$	**$7.7 \times 6.8 mm^2$**	$0.5 \times 0.5 \ mm^2$	$4 \times 6.5 \ mm^2$	NA		NA		$15 \times 7 \ mm^2$
Power cons.	0.92 mW	**1 mW[B]**	NA	0.5 mW	2.1 mW	9.4 mW	0.39 mW	0.09 mW	9.69 mW
Energy eff.	3.4 pJ/bit	**3.7 pJ/bit[B]**	NA	2 pJ/bit	20 pJ/b	90 pJ/b	19 pJ/b	4.4 pJ/b	5.8 pJ/bit

[A] Collision due to random access with TDM. [B] Includes three channels.
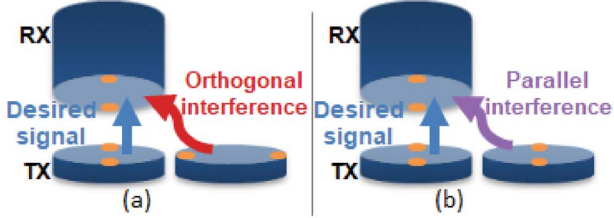
Fig. 14. The measurement setup utilizes a liquid phantom. The measurement consists of adjusting the TX's position to simulate interference emitted from a neighboring node. The analysis compares the interference from both orthogonal (a) and parallel (b) interferer configurations.
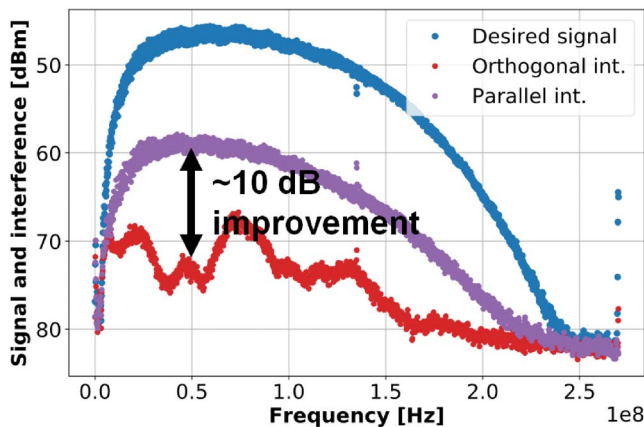
Fig. 15. The frequency spectrum of the desired signal, and the interferer for two configurations: orthogonal and parallel. The interferer is positioned at a distance of 8 mm from the desired TX.

C. Spatial Isolation Measurement

To validate the spatial isolation required for SDM in a multi-node network, a measurement with liquid phantom is conducted with a TX and a RX positioned as shown in Fig. 14(a) and 14(b). The TX is aligned with the RX, and the received signal is recorded as the desired signal. Then, the TX is repositioned to simulate the presence of an adjacent node emitting an interference signal. The measurements are conducted with the TX dipole coupler orthogonal to the RX dipole coupler (Fig. 14(a)) and with the TX dipole coupler parallel to the RX dipole coupler (Fig. 14(b)).

Fig. 15 illustrates the measured frequency spectrum of the three received signals. When the interferer is positioned 8 mm away from the TX with perfect alignment, the SIR in the parallel configuration is ~12 dB. Additionally, the graph indicates improved performance in the case of an orthogonal interferer configuration, showing an increase in SIR by ~10 dB compared to the parallel configuration. This measurement highlights the spatial isolation characteristic of the proposed galvanic coupling enabling the SDM even with the dense deployment of the implants.

V. DISCUSSION

The presented work demonstrates the first near-field galvanic coupling for transdural implant-to-implant communication supporting multi-node network telemetry for iBCIs applications. Table I compares the performance of the presented transceiver with the state-of-the-art transdural or transcranial telemetry and wideband BCC RXs. The presented RX consumes only 0.33 mW

per channel and has an input referred noise of 13.21 nV/$\sqrt{Hz}$, which is comparable to the state-of-the-art BCC RXs [33], while having an order of magnitude wider bandwidth, leading to a $> 10\times$ better energy efficiency of 1.24 pJ/bit.

Inductive coupling demonstrated in [2] has a miniature implant form factor of only 0.5mm $\times$ 0.5mm, but its data rate is limited to only 10 Mbps. Although capacitive BCC telemetry in [30], [33] has the potential to meet the size-bandwidth-power trade-off in the targeted application, it does not possess the spatial isolation required for SDM and is vulnerable to FM interference. The prior work of [14] based on the near-field galvanic coupling meets the target in implant size, bandwidth, and power consumption, but it does not include a corresponding high-bandwidth RX that can mitigate the misalignment and blind spot issues. The UWB implant-to-wearable transdural communication in [16] reaches a record 1.66 Gbps data rate. However, it consumes a $10\times$ higher power of $\sim$10 mW due to the need for a precise carrier frequency and phase control, which introduces a potential risk of tissue damage. In addition, the EM radiation-based UWB communication does not provide the spatial isolation required for SDM, which limits its employment in distributed scenarios with a high number of implant nodes.

As the primary focus of this work is on the high-bandwidth transdural wireless telemetry, the wireless powering method is not covered. However, since the proposed high-bandwidth wireless TX, together with high-channel-count intracortical neural sensors [6], can consume up to several mW of power, a power-efficient yet miniature wireless power transfer module that also satisfies the specific absorption rate (SAR) requirement is equally important. The recent advancement in ultrasound wireless power transfer in [34] demonstrates the feasibility of powering such free-floating implants with high power transfer efficiency and miniature form factor. Since the ultrasound wavelength is short in the body, the transducers can be on the millimeter scale. In addition, the SAR regulation is much more relaxed, i.e., 7.2 mW/mm^2 [35], making it a very promising transdural power transfer method for the targeted tether-less BCI applications.

VI. CONCLUSION

Existing iBCI systems with wired connections between the telemetry module and MEA can cause damage to brain tissue due to relative movements, scarring, and reduced longevity. The paper aims to design an untethered transdural telemetry network. The proposed 2TX-3RX transceiver topology with spatial diversity aims to mitigate misalignment issues and support SDM.

The RX covers a record wide bandwidth of 360 MHz. The measured high CMRR and low input-referred noise properties ensure effective signal preservation and reception. The ex-vivo validation using a 7-mm porcine tissue demonstrates a wireless communication with a data rate of up to 270 Mbps and a BER of less than 10^{-6}. The proposed 2TX-3RX topology provides the spatial isolation for the near-field galvanic coupled communication and improves the SIR by $\sim$10 dB, supporting spatial division multiplexing in the targeted multi-implant BCI telemetry networks.

The overall results support the efficacy of the proposed transdural BCC telemetry for distributed brain-wide telemetry networks, providing valuable insights for future applications and developments in implantable neural interface technology.

REFERENCES

[1] S. Saha et al., "Progress in brain computer interface: Challenges and opportunities," *Frontiers Syst. Neurosci.*, vol. 15, Feb. 2021, Art. no. 578875.

[2] J. Lee et al., "Neural recording and stimulation using wireless networks of microimplants," *Nature Electron.*, vol. 4, pp. 604–614, Aug. 2021.

[3] N. Ahmadi et al., "Towards a distributed, chronically-implantable neural interface," in *Proc. 9th Int. IEEE/EMBS Conf. Neural Eng. (NER)*, 2019, pp. 719–724.

[4] M. Zaeimbashi et al., "NanoNeuroRFID: A wireless implantable device based on magnetoelectric antennas," *IEEE J. Electromagn., RF, Microw. Med. Biol.*, vol. 3, no. 3, pp. 206–215, Sep. 2019.

[5] B. Chatterjee et al., "Biphasic quasistatic brain communication for energy-efficient wireless neural implants," *Nature Electron.*, vol. 6, pp. 703–716, Aug. 2023.

[6] N. A. Steinmetz et al., "Neuropixels 2.0: A miniaturized high-density probe for stable, long-term brain recordings," *Science*, vol. 372, no. 6539, Apr. 2021, Art. no. eabf4588.

[7] J. J. Jun et al., "Fully integrated silicon probes for high-density recording of neural activity," *Nature*, vol. 551, no. 7679, pp. 232–236, Nov. 2017.

[8] D.-Y. Yoon et al., "A 1024-channel simultaneous recording neural SoC with stimulation and real-time spike detection," in *Proc. Symp. VLSI Circuits*, 2021, pp. 1–2.

[9] D. A. Schwarz et al., "Chronic, wireless recordings of large-scale brain activity in freely moving rhesus monkeys," *Nature Methods*, vol. 11, no. 6, pp. 670–676, Jun. 2014.

[10] J. T. Schantz et al., "Cranioplasty after trephination using a novel biodegradable burr hole cover: Technical case report," *Neurosurgery*, vol. 58, no. 1 (Suppl), Feb. 2006, Art. no. ONS-E176.

[11] P. D. Wolf, "Thermal considerations for the design of an implanted cortical brain–machine interface (BMI)," in *Indwelling Neural Implants: Strategies for Contending With the in vivo Environment*, W. M. Reichert, Ed., Boca Raton, FL, USA: CRC Press, 2008. [Online]. Available: https://www.ncbi.nlm.nih.gov/books/NBK3932/

[12] E. Musk et al., "An integrated brain-machine interface platform with thousands of channels," *J. Med. Internet Res.*, vol. 21, no. 10, Oct. 2019, Art. no. e16194.

[13] X. Chen et al., "Chronic stability of a neuroprosthesis comprising multiple adjacent Utah arrays in monkeys," *J. Neural Eng.*, vol. 20, no. 3, Jun. 2023, doi: 10.1088/1741-2552/ace07e.

[14] C. Shi et al., "Galvanic-coupled trans-dural data transfer for high-bandwidth intracortical neural sensing," *IEEE Trans. Microw. Theory Techn.*, vol. 70, no. 10, pp. 4579–4589, Oct. 2022.

[15] Y. Feng et al., "Relative brain displacement and deformation during constrained mild frontal head impact," *J. Roy. Soc. Interf.*, vol. 7, no. 53, pp. 1677–1688, Dec. 2010.

[16] M. Song et al., "A 1.66Gb/s and 5.8pJ/b transcutaneous IR-UWB telemetry system with hybrid impulse modulation for intracortical brain-computer interfaces," in *Proc. Int. Solid-State Circuits Conf. (ISSCC)*, 2022, pp. 394–396.

[17] M. A. Callejón et al., "Galvanic intrabody communication for brain stimulation: A finite-element simulation study," in *Proc. MTT-S Int. Conf. Numer. Electromagn. Multiphys. Model. Optim. RF, Microw., THz Appl. (NEMO)*, 2017, pp. 19–21.

[18] B. Chatterjee et al., "A 1.15μW 5.54mm3 implant with a bidirectional neural sensor and stimulator SoC utilizing bi-phasic quasi-static brain communication achieving 6kbps-10Mbps uplink with compressive sensing and RO-PUF based collision avoidance," in *Proc. VLSI Circuits*, 2021, pp. 1–2.

[19] S. Gabriel et al., "The dielectric properties of biological tissues III. Parametric models for the dielectric spectrum of tissues," *Phys. Med. Biol.*, vol. 41, no. 11, pp. 2271–2293, Nov. 1996.

[20] J. Bae et al., "The signal transmission mechanism on the surface of human body for body channel communication," *IEEE Trans. Microw. Theory Techn.*, vol. 60, no. 3, pp. 582–593, Mar. 2012.

[21] Y. -J. Jeon et al., "A 0.034% charge-imbalanced neural stimulation front-end (SFE) IC with on-chip voltage compliance monitoring circuit and analysis on resting potential by utilizing the SFE IC," *IEEE Trans. Circuits Syst., Reg. Papers*, vol. 66, no. 10, pp. 3797–3810, Oct. 2019.

[22] K. H. Lee, P. S. Duffy, and A. J. Bieber, *Deep Brain Stimulation: Indications and Applications*. Singapore: Pan Stanford Publishing Pte. Ltd., 2016.

[23] M. Ortmanns et al., "A 232-channel epiretinal stimulator ASIC," *IEEE J. Solid-State Circuits*, vol. 42, no. 12, pp. 2946–2959, Dec. 2007.

[24] X. F. Wei et al., "Analysis of high-perimeter planar electrodes for efficient neural stimulation," *Frontiers Neuroeng.*, vol. 2, Nov. 2009, doi: 10.3389/neuro.16.015.2009.

[25] S. Maity et al., "BodyWire: A 6.3-pJ/b 30-Mb/s −30-dB SIR-tolerant broadband interference-robust human body communication transceiver using time domain interference rejection," *IEEE J. Solid-State Circuits*, vol. 54, no. 10, pp. 2892–2906, Oct. 2019.

[26] J. Mao et al., "Using human body as a monopole antenna for energy harvesting from ambient electromagnetic energy," in *Proc. Biomed. Circuits Syst. Conf. (BioCAS)*, 2017, pp. 1–4.

[27] H. Cho et al., "A 79 pJ/b 80 Mb/s full-duplex transceiver and a 42.5 μW 100 kb/s super-regenerative transceiver for body channel communication," *IEEE J. Solid-State Circuits*, vol. 51, no. 1, pp. 310–317, Jan. 2016.

[28] B. Kibret et al., "Characterizing the human body as a monopole antenna," *IEEE Trans. Antennas Propag.*, vol. 63, no. 10, pp. 4384–4392, Oct. 2015.

[29] D. Yang et al., "In-the-wild interference characterization and modelling for electro-quasistatic-HBC with miniaturized wearables," *IEEE Trans. Biomed. Eng.*, vol. 68, no. 9, pp. 2858–2869, Sep. 2021.

[30] J. Jang et al., "Wireless body-area-network transceiver and low-power receiver with high application expandability," *IEEE J. Solid-State Circuits*, vol. 55, no. 10, pp. 2781–2789, Oct. 2020.

[31] J. Bae and H.-J. Yoo, "The effects of electrode configuration on body channel communication based on analysis of vertical and horizontal electric dipoles," *IEEE Trans. Microw. Theory Techn.*, vol. 63, no. 4, pp. 1409–1420, Apr. 2015.

[32] M. A. Callejón et al., "Measurement issues in galvanic intrabody communication influence of experimental setup," *IEEE Trans. Biomed. Eng.*, vol. 62, no. 11, pp. 2724–2732, Nov. 2015.

[33] C. Lee et al., "A miniaturized wireless neural implant with body-coupled power delivery and data transmission," *IEEE J. Solid-State Circuits*, vol. 57, no. 11, pp. 3212–3227, Nov. 2022.

[34] M. Gourdouparis et al., "An ultrasound powering TX with a global charge redistribution adiabatic driving, achieving 69% power reduction and 53-degree maximum beam steering angle for implantable applications," in *Proc. ISSCC*, 2024, pp. 102–103.

[35] FDA, "Marketing clearance of diagnostic ultrasound systems and transducers; guidance for industry and food and drug administration staff," Rockville, MD, USA: Food and Drug Administration (FDA), Feb. 2023. [Online]. Available: https://www.fda.gov/regulatory-information/search-fda-guidance-documents/marketing-clearance-diagnostic-ultrasound-systems-and-transducers

Chengyao Shi (Graduate Student Member, IEEE) received the B.S. and M.S. degrees from the University of Padova, Padova, Italy in 2017 and 2020, respectively. He is currently working toward the Ph.D. degree with Eindhoven University of Technology (TU/e). He is also working in IMEC. His research interests include body area network and intrabody communication.

Yuming He (Graduate Student Member, IEEE) received the B.S. degree in optical information and technology from South China University, China, in 2012, and the M.S. degree in electronics engineering from Delft University of Technology, The Netherlands, in 2014. Since 2015, he has been with IMEC, The Netherlands, as a Researcher. Currently, he is also working toward the Ph.D. degree with the University of Groningen, Groningen, The Netherlands. His research interests include energy-and area-efficient sensing systems for implantable neural interfaces.

Marios Gourdouparis (Graduate Student Member, IEEE) received the M.Eng. degree from the National Technical University of Athens, Athens, Greece, in 2021. Currently he is working toward the Ph.D. degree with the Delft University of Technology (TU Delft), Delft, The Netherlands. He is currently with IMEC, Eindhoven. His current research interests include ASIC design and ultrasound powering for implantable applications.

Guido Dolmans received the M.Sc. and Ph.D. degrees in electrical engineering from Eindhoven University of Technology (TU/e), in 1992 and 1997. After receiving the Ph.D. degree, he became a Senior Scientist with Philips Research, from 1997 to 2006, before moving on to the position of the Scientific Director and a R&D Manager with IMEC Netherlands, from 2006 to present. In 2014, he returned to TU/e as a Full Professor, while continuing to work with IMEC Netherlands. His research interests include circuits and systems for wireless communications, localization, radar, AI, and data science. He has (co)-authored over 100 papers in scientific/technical journals and proceedings, and holds 14 U.S. patents.

Yao-Hong Liu (Senior Member, IEEE) received the Ph.D. degree from the National Taiwan University, Taiwan, in 2009. He was with Terax, Via Telecom (now Intel), and Mobile Devices, Taiwan, from 2002 to 2010, developing wireless transceiver ICs. Since 2010, he has been with IMEC, The Netherlands, and leads the research of the ultra-low power ASIC design. He is currently the Scientific Director with IMEC, and a Distinguished Research Associate with Technical University Eindhoven. He is a recipient of European Research Council (ERC) Consolidator grant. His research interests include wireless technologies for implantable brain–computer interfaces and IoT. He served as a Technical Program Committee of IEEE ISSCC and he is currently a Steering Committee Member of IEEE RFIC Symposium.